



Nanoscale Systems for Optical Quantum Technologies

Grant Agreement No: 712721

Start Date: 1st October 2016 - Duration: 36 months

D2.4 Single ion quantum memory

Deliverable:	D2.4
Work package:	WP2 Spin-atom-photon interfaces
Task:	2.1 Purcell-enhanced readout of a single Eu ³⁺ ion
Lead beneficiary:	KIT
Type:	Report
Dissemination level:	Public
Due date:	30 June 2019
Actual submission date:	26 September 2019
Author(s):	David Hunger (KIT)



This project has received funding from the European Union's Horizon 2020 research and innovation programme under grant agreement No 712721.

Version history

Version	Date	Author(s)	Description
V1	10/09/2019	D. Hunger (KIT)	First draft
V2	26/09/2019	D. Hunger (KIT) with inputs from the consortium	Revised version submitted to EU

Copyright Notice

Copyright © 2019 NanOQTech Consortium Partners. All rights reserved. NanOQTech is a Horizon 2020 Project supported by the European Union under grant agreement no. 712721. For more information on the project, its partners, and contributors please see <http://www.nanoqtech.eu/>. You are permitted to copy and distribute verbatim copies of this document, containing this copyright notice, but modifying this document is not allowed.

Disclaimer

The information in this document is provided as is and no guarantee or warranty is given that the information is fit for any particular purpose. The user thereof uses the information at its sole risk and liability.

The document reflects only the authors' views and the Community is not liable for any use that may be made of the information contained therein.

Table of Contents

Deliverable Description	4
Results	4
1. <i>Custom-designed cryogenic scanning cavity stage v1</i>	4
2. <i>Improved cavity-enhanced ensemble spectroscopy</i>	6
3. <i>Improved custom cavity stage v2</i>	7
4. <i>Reference cavity</i>	8
5. <i>Fiber background light</i>	9
6. <i>Nanoparticle sizing and thin film embedding</i>	9
7. <i>Prospect for single ion detection</i>	11
7.1 <i>Cavity-enhanced fluorescence detection</i>	11
7.2 <i>Cavity-enhanced absorption detection</i>	12
8. <i>Modelling of ion-cavity interactions and readout</i>	15
Summary and Outlook.....	16
References.....	17

Deliverable Description

This deliverable describes the work on task 2.1, which has the goal of detecting single Eu^{3+} ions by cavity-enhanced spectroscopy and using them as an optically addressable quantum memory. Building on the results reported in D1.1, D1.5 and D2.2, we could improve cavity-enhanced spectroscopy and observed statistical fine structure of small ion ensembles. Experimental limitations such as mechanical vibration noise in the cryostat, fiber background fluorescence, and laser frequency instability were identified, and ways for their solution are presented. Extended sample characterization and thin film embedding of nanoparticles are presented. Finally, two different approaches towards single ion detection are analysed, and modelling of ion-cavity coupling and efficient quantum state readout is presented. While the partially unforeseen difficulties described here hindered us to achieve single ion detection and control, progress on various aspects of the task could be made, and important insights gained.

Results

We describe in the following the progress towards single Eu^{3+} ion detection and control in different subchapters. We begin by summarizing the technical status of the central experimental device, the cryogenic cavity platform. It was one of the main efforts of the project to develop a custom-designed nanopositioning platform that can be operated in a closed cycle cryostat, and we summarize here the achieved performance of a first version (v1) of the device. We then report cavity-enhanced spectroscopy of ion ensembles performed with the cavity stage v1, in particular the observation of statistical fine structure. We then continue with the developments to improve the cavity stage, and first results of a second version (v2) are reported. We proceed by presenting work towards laser frequency stabilization with a reference cavity and discuss limitations due to fiber background light. Furthermore, we describe a promising approach for cavity integration of nanoparticles by thin film embedding. Finally, we analyze the prospects for single ion detection by cavity-enhanced fluorescence and absorption spectroscopy and summarize work on modelling ion-cavity coupling and efficient quantum state readout.

1. Custom-designed cryogenic scanning cavity stage v1

As initially reported in D1.1, the operation of a high finesse tunable microcavity in a closed-cycle cryostat was not compatible with the use of commercially available nanopositioning stages, and a custom-designed scanning cavity stage was developed during the project. D1.1 describes the design and the characterization of a first realization, including active length stabilization under ambient conditions without cryostat. D1.5 reports on results of operating a cavity with finesse 20000 including scanning and stabilization, with full thermalization and passive mechanical decoupling in the cryostat. Thermalization was achieved down to sample temperatures of 9K, and Pound-Drever-Hall locking achieved a length stability of 0.6pm rms at room temperature with the cryostat turned off. The noise increased to 4pm rms at elevated temperature when the cryostat was running, and to 60pm rms for a running cryostat and $T=12\text{K}$. Figure 1a) shows noise amplitude spectra taken for the three described situations. The noise level corresponds to a 100-fold improvement of stability compared to the earlier used commercial nanopositioning platform.

Improved stability could be achieved recently when the cavity fiber was brought into direct mechanical contact with the planar mirror. Figure 1b) shows noise spectra with mechanical contact taken either at $T=12\text{K}$ with the cryostat running (yellow line) or the cryostat switched off for a few minutes during the measurements, leading to a temperature of about 15K . The noise decreased from 60pm to 7pm rms in contact, and to 0.3pm in contact with the cryostat turned off. This stability would be sufficient for experiments, also at higher finesse than currently used. In the test, the cavity was resonant with one laser source, but for spectroscopy we require locking light at 690nm and probe light at 580nm to be simultaneously resonant. While this is not compatible with contact mode for one cavity, it is expected that a setup containing two cavity fibers next to each other, one for locking and one for spectroscopy, should allow the combination of contact mode and locking at a different wavelength. Such a system is currently under preparation.

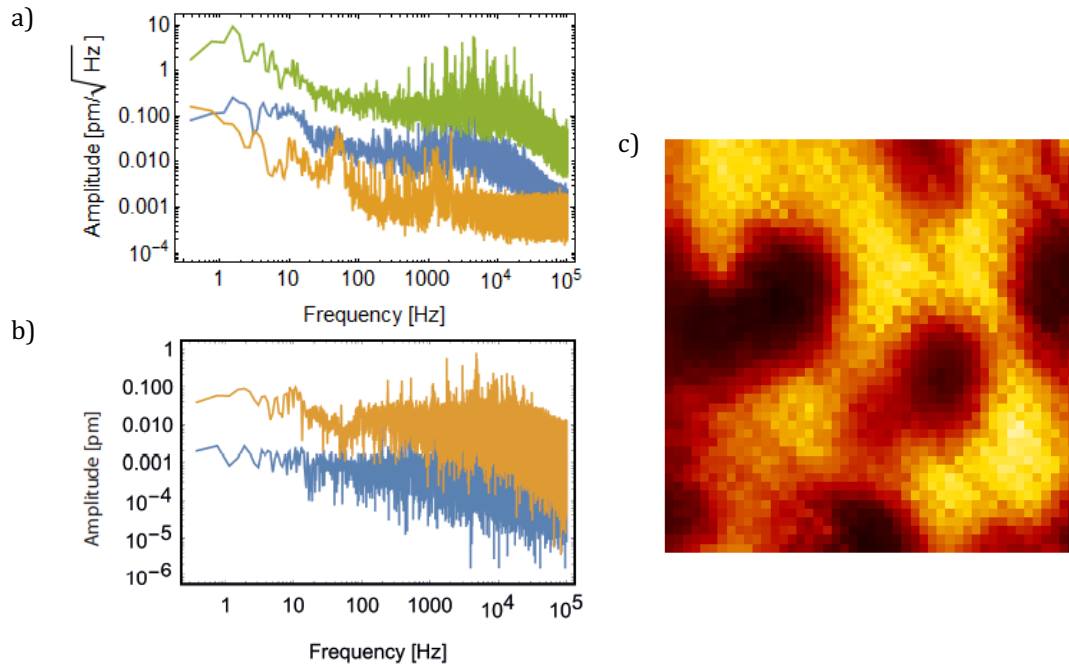


Figure 1: a) Amplitude noise spectral density of cavity length fluctuations of the locked custom cavity stage v1 (yellow: cryostat off; blue: cryostat running, close to RT; green: cryo running at 12K). b) Noise spectra for a cavity in mechanical contact (blue: cryo off, 15K , yellow: cryo running, 12K). c) Scanning cavity transmission map of scattering loss from isolated $\text{Eu}^{3+}:\text{Y}_2\text{O}_3$ nanocrystals on a $\sim 10 \times 10 \mu\text{m}^2$ area.

To localize suitable nanocrystals inside the cavity mode, piezo-based fine tuning and motor-driven coarse positioning was implemented and brought into operation also at low temperature. Figure 1c) shows a scanning cavity transmission measurement of isolated $\text{Eu}^{3+}:\text{Y}_2\text{O}_3$ nanoparticles at 8K . Chapter 2 describes spectroscopy experiments performed with this platform.

Since the performance was still not fully meeting the requirements for optimal operation, we designed and realized an improved version of the custom cavity stage. Details on the progress are described in Chapter 3.

2. Improved cavity-enhanced ensemble spectroscopy

We performed spectroscopy of Eu doped nanocrystals with the custom cavity stage. Experiments analogous to the ones reported in D2.2 were conducted, where we excited ions via the coherent 7F_0 - 5D_0 transition at 580nm and collected cavity-enhanced emission at 611nm. The signals reported in D2.2 Fig. 5 could be reproduced for fluorescence detection via the 611nm transition, and a reduction of the required integration time was achieved. A more careful analysis of the count rate enhancement as the one reported in D2.2 yields an effective Purcell factor of 2, consistent with a calculation based on the involved transitions, their oscillator strengths and linewidths (the results of D2.2 were published in [Casabone08], see there for more details). The achieved signal to background ratio in the new measurements remained however essentially unchanged. With this we were limited at approximately the same excitation power level as in the earlier experiments, such that again signals from about 10 ions were probed for a signal-to-noise ratio close to 1.

To identify spectral structure in the inhomogeneous line originating from the statistical frequency distribution of the ions, we performed cavity-enhanced spectroscopy at different excitation powers and studied the noise of the ensemble spectral line. We observed structure in the noise that reproduced over several measurements, characteristic of statistical fine structure of a small ensemble. Due to the statistical nature of the ion spectral density, a fluctuation of $\delta N_{ion} = \sqrt{N_{ion}}$ is expected, which directly translates into a corresponding noise in the intensity of the inhomogeneous line. Figure 2 shows measurements at three different intra-cavity excitation intensities (2×10^{-4} GW/cm², 1×10^{-2} GW/cm², 1×10^{-1} GW/cm²),

where the fluorescence intensity was normalized to the peak count rate for comparison. The yellow marked structures repeat in all measurements in a statistically significant manner and are indicative of fine structure in the ion spectral density. We observe noise of 20 – 30% (peak-peak), consistent with a fine structure originating from a number of 10 – 30 ions per spectral bin, in accordance with the evaluation from power broadening (see D2.2 and [Casabone18]). However, the different power levels do not change the contrast as strongly as expected. This hints towards unresolved finer spectral structures which are not probed consistently in all measurements, and experiments with smaller laser frequency steps are required. At the time of the experiment, the probe laser was free running, and frequency drifts of a few MHz over the time of the measurements are present. For more reproducible measurements that enable single ion spectral lines to be resolved, active stabilization of the laser frequency and laser line narrowing are required.

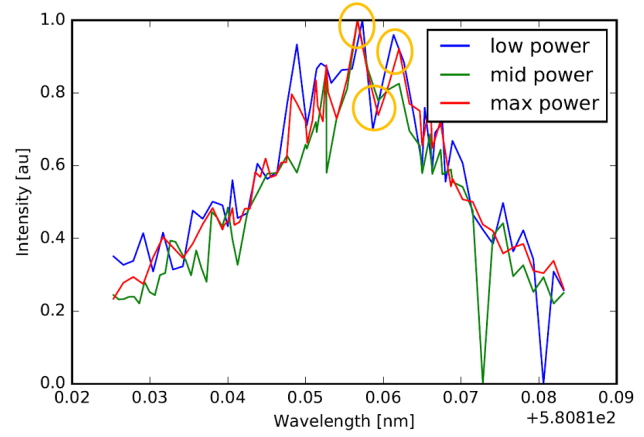


Figure 2: High-resolution cavity-enhanced spectroscopy of the inhomogeneous line of an isolated $\text{Eu}^{3+}:\text{Y}_2\text{O}_3$ nanocrystal. The excitation laser wavelength was scanned around the 7F_0 - 5D_0 transition and cavity-enhanced emission at 613nm via the 5D_0 - 7F_2 transition was recorded for different excitation intensities (red: 0.2MW/cm², green: 10MW/cm², blue: 100MW/cm²).

Therefore, we have designed and started to build an ultra-stable reference cavity. Details of this are described in Chapter 4.

To make use of the maximal Purcell enhancement, we have also tried to detect the 580nm emission of the ions coupled to the cavity. Therefore, we used an AOM to create $\sim 10\mu\text{s}$ long pulses for excitation and a shutter wheel to completely block excitation light that may enter the experiment outside the pulse window. To detect the ion signal, we gate the APD and record the time-delayed emission after a waiting time of 100 – 200 μs . In such measurements, we observe a significant long-lived background, and so far, no signals from ions could be detected. Chapter 5 gives more details on the background measurements.

3. Improved custom cavity stage v2

The strong increase of mechanical noise observed with the cavity at low temperature, which included particularly high frequencies up to 50kHz, is expected to originate in part from a stiffening of the used mechanical decoupling components. Also, we observed substantial misalignments (several 100 μm) of the cavity during cooldown, requiring manual compensation of position shifts during the entire cooldown time. Furthermore, we were not able to achieve temperatures below 7K. We thus redesigned the platform and introduced several improvements:

- mechanical decoupling of the cavity stage from the cryostat cold plate with springs to suppress the transmission of high frequency vibrations
- choice of titanium for the main body to match the thermal expansion of the stage with the used piezo actuators. This should minimize alignment changes during cooldown.
- choice of copper for radiation shield parts to improve thermalization
- improved thermal connections with flexible copper braids that minimize mechanical coupling
- improved mechanical design to avoid misalignments induced by thermal contraction

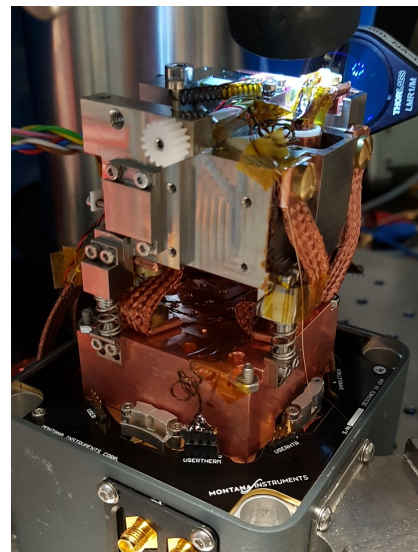


Figure 3: Improved custom cavity stage built into the crystat.

The improved scanning cavity platform was integrated into the cryostat and tested. At a first cool down, a sample temperature of 10K was achieved. Improvements on thermal contacts are expected to allow for further improvements. Active stabilization of the cavity was tested outside the cryostat with a simplified lock using a Red Pitaya FPGA and the PyRPL software package. An integrated length instability of 1.2pm was achieved, dominated by detector noise and a noise peak at 18Hz and harmonics, which corresponds to the eigenfrequency of the springs.

After integration into the cryostat, active stabilization was tested and first locking was achieved, however not yet at optimized performance. Alignment changes during cooldown were reduced by up to 10-fold compared to the earlier stage v1.

We have thus achieved improved operation of the cavity at a level that can now be expected to be suitable to perform spectroscopy experiments.

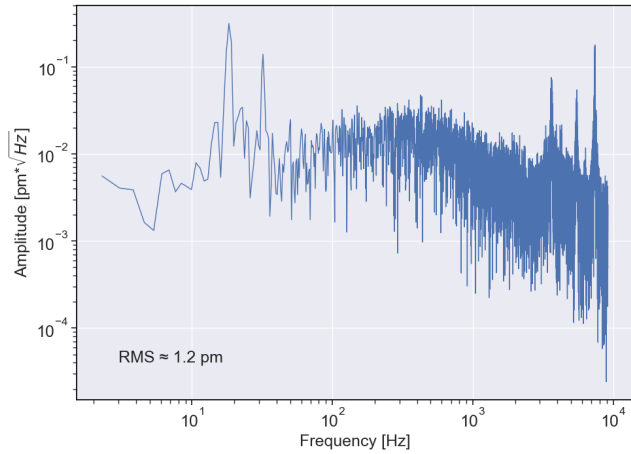


Figure 4: Vibration noise amplitude spectral density of the improved custom cavity stage mounted on an optical table and actively stabilized with an FPGA side-of-fringe lock, yielding 1.2pm rms noise.

4. Reference cavity

We have designed and machined an ultra-stable reference cavity to stabilize the laser frequency following the design described in [Brachmann12, Alnis08]. The core part consists of a Zerodur spacer with an exceptionally low thermal expansion coefficient ($< 10^{-7}/K$) onto which two cavity mirrors are attached. The spacer is mounted vertically inside a vacuum chamber by Nylon screws to minimize vibration coupling, and is enclosed by a double thermal shield to minimize impact from blackbody radiation and temperature variations of the outside. The temperature of the inner shield is actively stabilized with a Peltier element. The targeted cavity linewidth is $\sim 100\text{kHz}$, and the cavity mode spectrum is chosen such that no overlap of the fundamental Gaussian mode with higher order transverse modes is expected. This design has achieved a laser linewidth of 500Hz and drifts of $< 50\text{Hz/s}$ [Brachmann12] and was shown to ultimately achieve sub-Hz linewidth and drift with further improvements [Alnis08]. All parts have been prepared (including mechanical parts, optics, locking electronics), and the system is currently assembled and taken into operation.

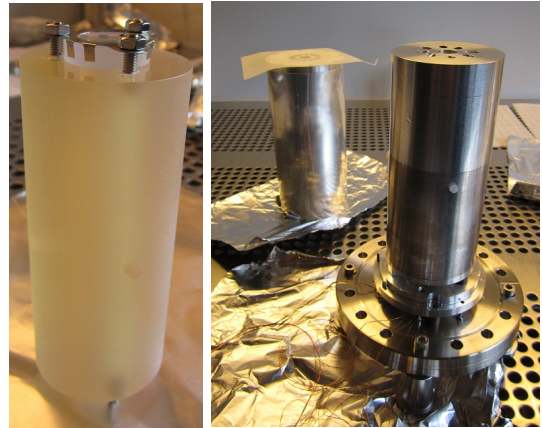


Figure 5: Photograph of the Zerodur spacer with mounted mirrors (left) and parts of the radiation shield and the vacuum chamber (right).

5. Fiber background light

We found that one of the limiting factors for the achievable signal to noise ratio is background light of the cavity fiber and of the cavity mirror, originating both from autofluorescence and Raman scattering. The excitation light propagates over $\sim 2\text{m}$ in the cavity fiber and can produce background light there. While the final coherent spectroscopy of single ions will be operated at very low power (sub nW) such that no background issues are expected, searching for a signal needs to be done in the power broadening regime with few hundred μW excitation power, where hundreds of kCts background is observed. We have performed fluorescence measurements with pulsed excitation and time delayed detection at the excitation wavelength. We observe a long-lived background contribution with a time constant of up to 4ms, which spectrally and spatially overlaps with the ion fluorescence.

Since this background has hindered us so far to observe ion signals, we have compared the background level of different fibers. Figure 6 shows a spectrum with characteristic Raman and fluorescence contributions (a), and a non-linear power dependence of the background (b). We find that pure silica core fibers have an up to 5x lower background compared to the currently used Ge doped fibers. New cavity fibers will thus be prepared from pure silica fibers in the future.

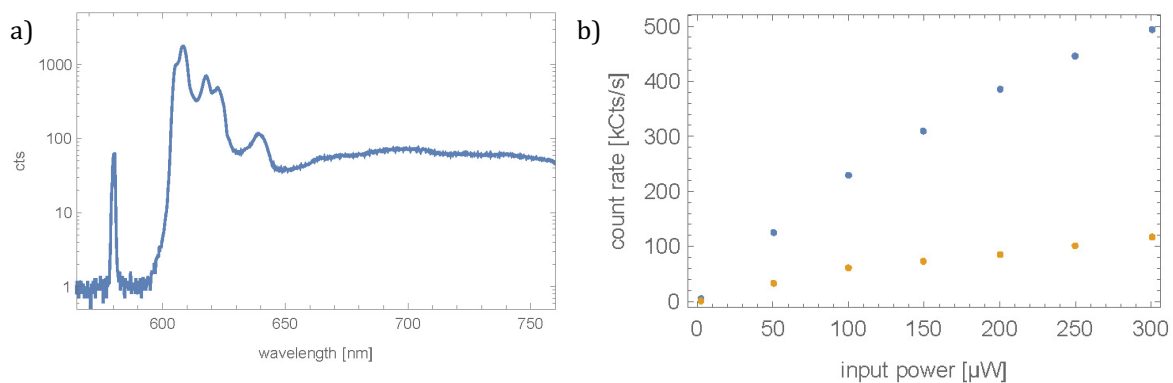


Figure 6: a) Spectrum of the fiber background signal (Ge doped SM450 fiber) in logarithmic scale, excitation at 532nm and long pass filtering with a cutoff at 600nm. The structure between 600 - 650nm is attributed to Raman scattering, the broad background to fluorescence. b) Comparison of a Ge doped (blue) and a pure silica fiber (yellow).

6. Nanoparticle sizing and thin film embedding

As described in D1.1 and D2.2, nanocrystals placed inside the cavity lead to Rayleigh scattering loss that can become dominating for crystal size $> 60\text{nm}$. At the same time, a nanocrystal reduces the local electric field inside and yields a prolonged excited state lifetime and a reduced coupling to the cavity field. Both aspects can be improved when embedding nanoparticles in a thin film which ideally is index matched. We performed simulations and measurements and identified an optimized approach to integrate doped nanocrystals into the cavity.

As a first step, we analyze nanocrystal samples spin-coated on reference substrates and cavity mirrors to obtain reference values for optical properties. We study a large number of isolated nanocrystals by confocal microscopy and infer the peak count rate per crystal under saturation conditions, see Figure 7a.

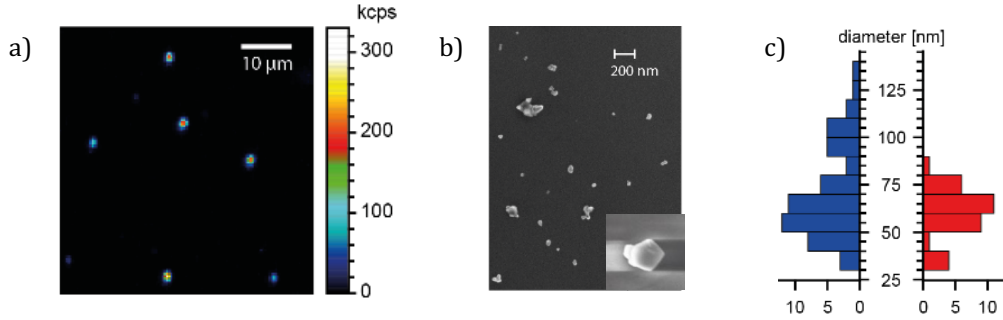


Figure 7: a) Confocal fluorescence image of individual nanocrystals spincoated on a mirror. b) SEM image of isolated nanocrystals dispersed on a substrate. c) Histogram of measured crystal sizes (right panel, red bars) and histogram of calculated crystal sizes from a measured fluorescence distribution (left panel, blue bars).

By looking at the count rate distribution and comparing with a size distribution obtained from SEM images such as the one shown in Figure 7b, we can get an order of magnitude estimate for the typical count rate per single ion. Figure 7c shows a histogram of the measured crystal size (red, right) and the expected crystal size distribution calculated from the measured fluorescence values (blue, left). Here we assume that the count rate R and crystal radius r are directly related via $R = N R_0 = \left(\frac{4\pi}{3}\right) n_0 r^3 R_0$, where R_0 is the single ion count rate and N the number of ions. From the size and doping concentration, and knowing that the Y concentration in the C_2 site is $n_0 = 1.6 \times 10^{22} / \text{cm}^3$, single crystals of e.g. 60nm diameter contain $N \sim 10^4$ ions. The two distributions match if we assume an excited state population of 20% (several ground state levels are thermally populated, but only one is excited at about one saturation intensity) and an overall fluorescence detection efficiency of 1.5%. This value is smaller than the expected maximally achievable detection efficiency of 20% for our setup, which we calculate from the modified dipole emission pattern on a Bragg mirror averaged over dipole orientations, the angular collection efficiency of the microscope objective, the maximal transmission through the optics, and the detector quantum efficiency. The smaller experimental value is ascribed to suboptimal collection and transmission efficiency and a potential overestimation of the excited state population. The analysis shows that we detect about 2 photons per second per ion. This value can be compared to cavity-enhanced measurements described above, where we estimate signals of ~ 30 photons per second per ion. The count rate increase in the cavity originates both from a lifetime change and improved photon collection efficiency.

As a second step, we studied embedding into a combined SiO₂ / PMMA layer whose thickness was matched to achieve a large electric field inside the film, see Figure 8 a). Analytic calculations and numerical simulations yield that the scattering loss can be reduced by up to a factor 6.7, and that the excited state lifetime can be reduced by up to a factor 3.8.

We experimentally studied these effects for our sample. Figure 8 b) shows fluorescence lifetime measurements as function of the count rate for crystals prepared in two different ways. First, the particles are spin coated onto a fused silica substrate to serve as a reference (blue data). Second, we embed the particles into a SiO₂/PMMA layer on top of a dielectric mirror (yellow). We observe a correlation between lifetime and count rate for both samples, and a reduced lifetime for the embedded particles. The blue line for the reference sample is an analytical calculation of the excited state lifetime [LeKien00] and a crystal size that is derived from the expected dependence of brightness and crystal size as described above. More details can be found in [Casabone18]. The measurements thus confirm the beneficial effect of embedding.

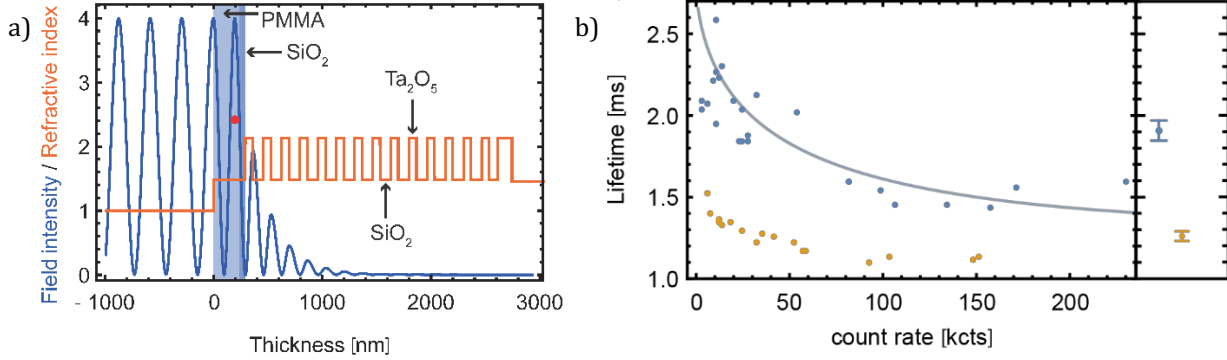


Figure 8: a) Refractive index profile (orange) of the mirror and electric field distribution (blue) for an embedded nanocrystal. b) Fluorescence lifetime as a function of the photon count rate. Each datapoint corresponds to a randomly chosen isolated crystal. The blue solid line is a fit to a model. Blue: crystals on glass. Yellow: Embedded crystals. The right panel shows the average lifetime and standard deviation for both cases.

Currently we work on optimizing this approach by embedding the nanocrystals in an index-matching Y₂O₃ thin film. First tests thin films have been grown by CNRS with CVD for parameters that are compatible with growth on a cavity mirror. Surface roughness measurements with AFM yielded 0.5nm rms, sufficient to avoid excessive scattering loss. We also studied background fluorescence from the films and found broad spectra peaking around 650nm and an integrated count rate of 1kCt/μW, similar to the value for the fiber.

7. Prospect for single ion detection

7.1 Cavity-enhanced fluorescence detection

Based on the results presented above, we give here an estimation on the achievable signal for resonant detection of single Eu ions and the expected fidelity that can be achieved for single qubit state preparation and readout.

Pulsed excitation with time-delayed fluorescence detection can be performed at a repetition rate of $\Gamma \approx \frac{\gamma_c}{3} = \frac{c\gamma_0}{3} \approx 5$ kHz for the currently achieved parameters ($F = 20000$, $Q = 10^5$, $V_c = 4\lambda^3$, $C = 15$). With an estimated overall detection efficiency (including cavity outcoupling, optics transmission & detector quantum efficiency) of 10% as achieved in earlier experiments, this leads to signal rates of 500Hz, significantly larger than the APD dark count rate of 20Hz.

Preparation of quantum states can be performed by a pair of complex hyperbolic secant two-color pulses [Roos04, Rippe08] that allow one to perform arbitrary rotations on the Bloch sphere with insensitivity to the Rabi frequency and detuning. Such pulses have been used to realize quantum states with Pr³⁺ ensembles with a fidelity >90% [Rippe08]. In

principle, higher fidelity can be expected for single Eu^{3+} ions due to the absence of ensemble inhomogeneities and a larger available bandwidth due to larger hyperfine splittings in Eu^{3+} . Including the required pulses for state tomography, overall fidelities $>80\%$ can be expected for the currently achieved parameters.

7.2 Cavity-enhanced absorption detection

As an alternative approach, cavity enhanced absorption spectroscopy is considered. This approach has several advantages. First, it is unaffected by parasitic fluorescence background, it is not limited by detector dark counts, and it can be debugged more easily due to the presence of a probe laser which can be set to higher power initially. In general, for an absorbing system described by an extinction cross section σ placed within a cavity with mode cross section πw_0^2 and Finesse $F = 2\pi/L_c$, the introduced round trip loss is given by $A = 4\sigma/(\pi w_0^2)$ and the resonant cavity transmission is given by $T = L_c^2/(L_c + 2A)^2$. For a rare earth ion with branching ratio ζ into the coherent transition of interest, the homogeneous linewidth γ^* broadened by dephasing, and the Fourier-limited linewidth γ , the extinction cross section is estimated to be

$$\sigma \approx \zeta \sigma_0 \frac{\gamma}{\gamma^*} = \frac{\zeta 3\lambda^2 \gamma}{2\pi \gamma^*} \approx 3 \text{ nm}^2.$$

The numerical value is estimated for Eu^{3+} with experimentally measured $\zeta = 1/100$ and $\frac{\gamma}{\gamma^*} = 3 \times 10^{-3}$ for the currently used sample. With the currently used cavity with $F = 20000$, $w_0 = 1.5\lambda$, this would lead to a change in resonant cavity transmission by $\sim 10\%$.

Treating the system as a two-level system subject to excessive dephasing coupled to the cavity yields a slightly different description based on the Purcell factor $C = \zeta 3\lambda^3 Q/(4\pi^2 V)$. The single ion extinction originating from the destructive interference of the field scattered by the ion and the probe laser leads to a cavity transmission amplitude [Auffeves07]

$$t_c = \frac{1}{1 + i\Delta_a/\kappa} \left(-1 + \frac{C \frac{\gamma}{\gamma + \gamma^*}}{C \frac{\gamma}{\gamma + \gamma^*} + \left(\frac{i\Delta_a}{\gamma + \gamma^*} + 1 \right) \left(\frac{i\Delta_c}{\kappa} + 1 \right)} \right).$$

Here, the cavity decay rate κ and the detuning Δ_a from the ion resonance and Δ_c from the cavity resonance are included. Figure 9 shows a calculation of the intensity transmission of the coupled cavity – ion system for $F = 80000$, $w_0 = 1.5\lambda$, $\gamma^* = 2\pi \times 20\text{kHz}$, which are parameters for an improved cavity and an improved material, similar to the best values observed to date. This motivates that nearly full extinction can be achieved with realistic experimental parameters. Such a behavior can be used for highly efficient single ion detection, single-shot state readout, and to create ion-photon entanglement.

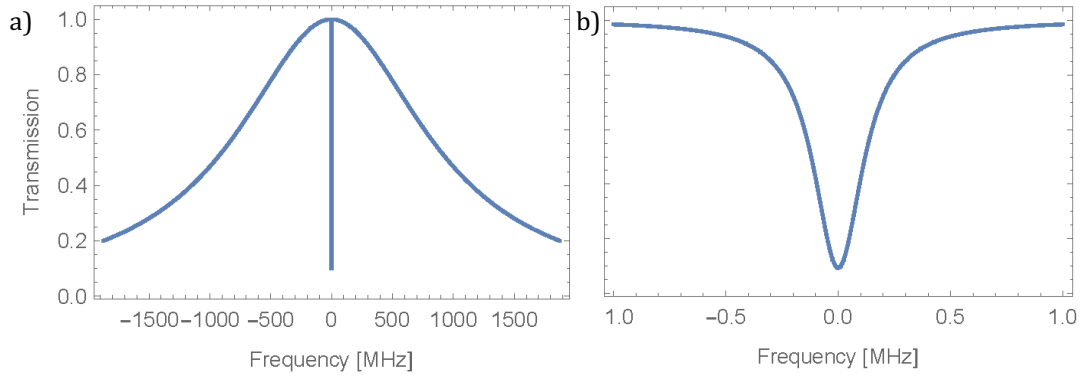


Figure 9: a) Calculation of the transmission of the coupled cavity-ion system with the ion resonant to the cavity and the laser frequency swept. The calculation is simplified in assuming only a two-level system and not the full 6-level structure. b) Zoom into the ion extinction resonance.

Cavity transmission noise

To investigate the feasibility of single ion detection already in the currently available scenario, we have performed extensive scanning cavity absorption measurements. First, the detection limit of measurements on a single spatial location on the planar mirror was investigated. Therefore, the cavity transmission resonance is repeatedly probed by a narrow-band laser by modulation of the cavity length, and the noise of the maximum transmission value is inferred. Here, a cavity finesse of $F = 40000$ was used in the experiment. The standard deviation of repeated measurements ranges between 0.3% and 2%, depending on the measurement rate and the overall stability of the system, which we trace back to phase noise originating from parasitic interferometers in the setup. The observed noise would be enough to achieve single ion extinction detection with $\text{SNR} \sim 5$, however only for an ideal coupling situation. Typically, more signal overhead is required for reliable measurements.

Averaging

Higher SNR can be achieved when averaging multiple measurements. Figure 10a shows a measurement of the Allan deviation of the cavity transmission peak amplitude sampled with a rate of 10 kHz. We find that the measurement uncertainty first decreases proportional to $t^{-1/2}$, as expected for uncorrelated white noise. For longer times, it increases linearly with time, a signature of continuous drifts, with additional minor parts of a random walk $\propto t^{1/2}$. This can be tracked back to laser intensity noise and other drifts in the experiment. Here, we achieve a lowest uncertainty of the cavity peak transmission of 2×10^{-4} within 0.2 s, corresponding to 2000 measurements.

Rapid referencing

To avoid the effect of slow drifts, rapid referencing can be used, i.e. a continuous comparison of the empty cavity and the sample inside at high speed. To test this compensation, a small area scan (16x16 points on an $5 \times 5 \mu\text{m}^2$ area) was repeated 1000 times with ~ 900 points/sec. In Fig. 10 b, the Allan deviation of two locations in this scan is evaluated. While the Allan deviation of the two individual spots increases after 10 sec due to intensity fluctuations, their ratio decreases further and is insensitive to the drifts. A total 70 sec long measurement of a whole scan yields an Allan deviation of 9×10^{-4} ,

without limitations due to drift. We conclude that further averaging could yield even lower values.

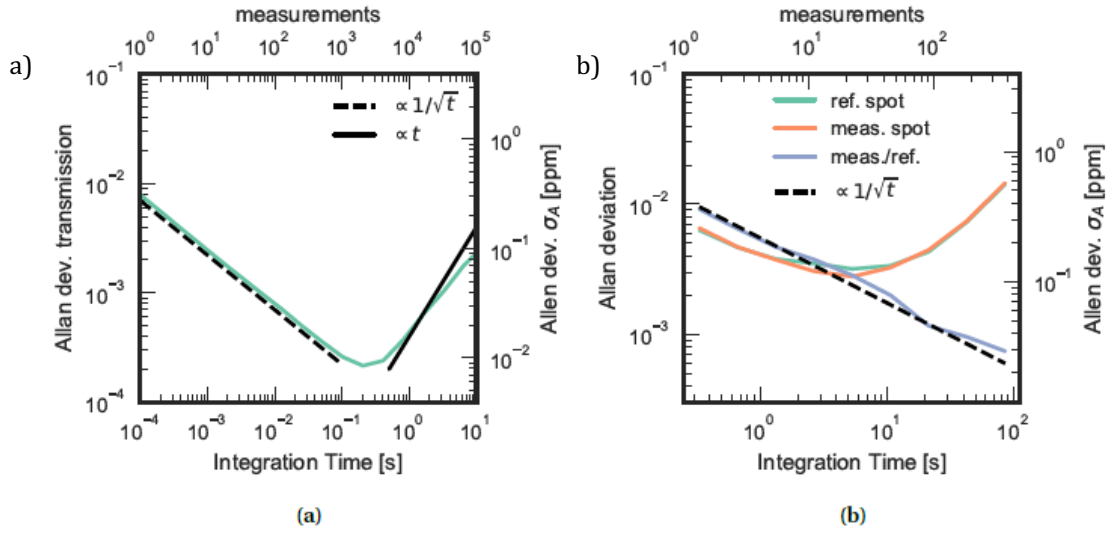


Figure 10: a) Measured Allan variance of the cavity transmission for repeated measurements at 10kHz measurement rate. b) Allan variance for a background subtracted measurement. Green: Reference spot. Orange: Measurement spot. Blue: Background-subtracted signal.

Background artefacts

Spatial referencing as described above is the typical approach to locate the sample, and we have developed scanning cavity microscopy (SCM) as a versatile tool to perform spatially resolved extinction microscopy. We studied the limit of this technique originating from spatial inhomogeneities of the cavity transmission signal. In different experiments using various mirror coatings, cavity geometries, and wavelengths, we consistently observe two classes of artefacts in SCM images that act as a limiting background noise, see Figure 11a): (ii) spatially localized contour lines with deteriorated cavity performance for certain longitudinal mode orders, and (iii) weak periodic background patterns. From detailed measurements and analyses we could derive that the localized structures (ii) originate from a spatial variation of resonant transverse-mode coupling (see Figure 11 b,c) and arise from the topography of the planar mirror surface, in particular its local curvature and gradient. We further examined the background patterns (iii) and found that they derive from non-resonant mode coupling, and we attribute it to the micro roughness of the mirror. From this analysis we find that optimally shaped concave micro mirrors and improved planarity of the planar mirror could reduce the effects of spatial inhomogeneity. Also, we have accurately modeled the cavity mode structure to be able to predict longitudinal cavity modes where artefacts have minimal influence. Mode orders were identified where artefacts lead to a transmission noise < 1%. Also, we have performed measurements at different wavelengths and found that artefact (iii) remains unaffected. This means that performing laser frequency sweeps together with scanning cavity microscopy, i.e. hyperspectral imaging, can be used to subtract this modulation. The results have been recently accepted for publication in New Journal of Physics [Benedikter19].

With these results, single ion extinction is expected to provide good SNR despite the presence of various noise sources and represents a promising route.

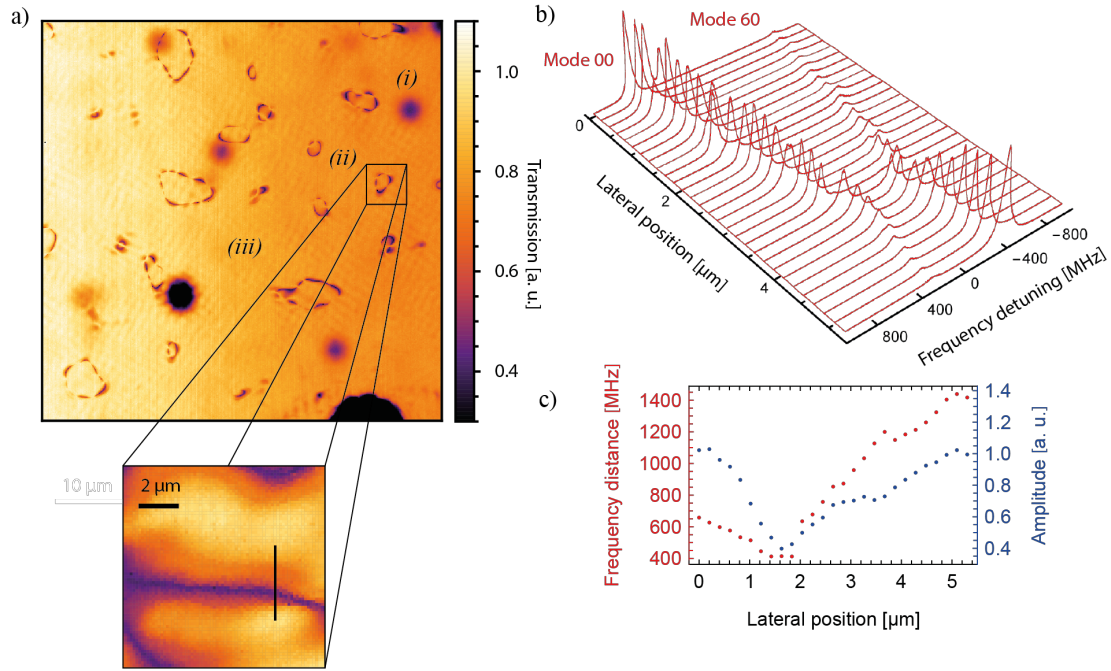


Figure 11 a) Scanning cavity transmission scan of a $100 \times 100 \mu\text{m}^2$ area at longitudinal mode order $q=15$ of a cavity with $F=60000$, $w_0 = 2 \mu\text{m}$. (i) Loss introduced by a nano-scale particle yielding the Gaussian point spread function of the fundamental cavity mode. (ii) Contour line of resonant mode coupling. (iii) Periodic background pattern. A close up around one contour line is shown in the panel below. (b) Cavity transmission spectra around the fundamental mode for different lateral positions on the path in the lower panel of (a) showing an avoided crossing with mode TEM(6,0). The minimal frequency separation is found at the darkest spot on the path in (a). (c) Maximal amplitude of the spectra in (b) (blue) and frequency separation $\Delta\nu_{\{00,60\}}$ of the two modes (0,0) and (6,0) along the path.

8. Modelling of ion-cavity interactions and readout

AU has developed theory to detect and manipulate two-level emitters through their interaction with probe fields injected in cavities. Previous to NanOQTech, we thus developed schemes to analyze homodyne reflection signals from a microwave cavity and infer the presence or absence of resonant emitters. Within NanOQTech, we have extended these theories to photon counting, and while we confirm the above estimates for the uncertainty of the scheme, our analyses permit assessment of the role of statistical correlations in the signal. It is thus possible to solve an efficient conditional master equation for the emitters from which a Bayesian analysis yields the most accurate assessment of the presence of the emitter.

In the bad cavity limit one can eliminate the cavity field from the theory and we have obtained the corresponding approximate conditional master equation and verified the agreement of the exact and approximate methods in the bad cavity limit [Lia18].

We have also incorporated the possibility that an emitter undergoes transition frequency fluctuations, see Figure 12, and shown that a Bayesian analysis of the probing trajectory yields a good estimate of the time varying field [Lia18].

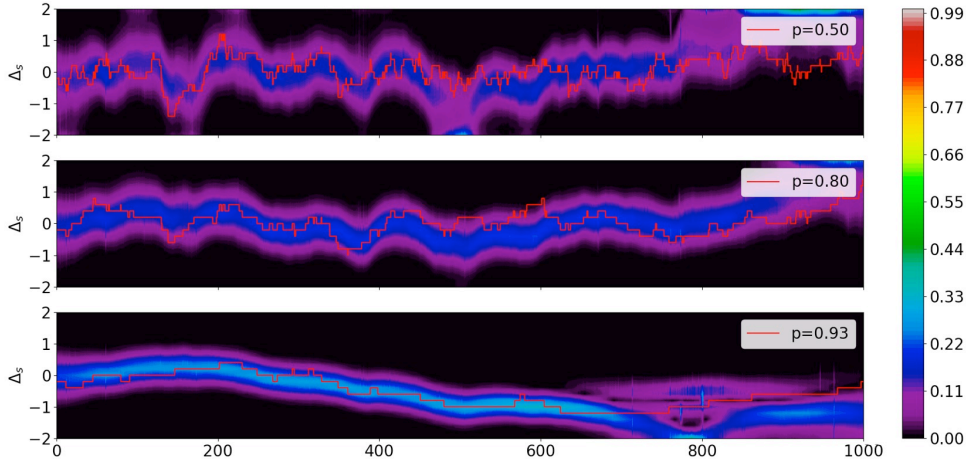


Figure 12: A fluctuating detuning of an emitter in a cavity is estimated from the detection record of light reflected from the cavity. In the simulation the red curve shows the true detuning, while the purple towards blue colors show the estimated probability distribution inferred from the signal and a “forward-backward” analysis (p is the detector efficiency).

The possibility to study superradiance and subradiance effects for multiple emitters in the cavity led to our separate analysis of multi-ion-cavity interactions. We have thus developed effective methods to analyze the dynamics of large ion ensembles with inhomogeneous broadening and to answer the pertinent question if ions with different frequencies operate collectively. In previous works we have shown that weakly interacting ions dephase independently, but with the small cavities in NanOQTech, the interactions may be stronger, and we indeed find that ions with relative detunings even orders of magnitude beyond the cavity linewidth perform synchronized Rabi oscillation [Synch19]. These results may also apply to the study of superradiant lasing with ultra-narrow linewidth atomic systems [Suplas18, Suplas19].

Summary and Outlook

Overall, we have advanced the spectroscopy of small ion ensembles, achieved Purcell enhanced spectroscopy of about 10 ions in an improved experimental system, and identified statistical fine structure. Several improvements of the setup have been implemented and initiated. While some unexpected challenges were identified that required more work than initially planned, we have been able to make progress to overcome them, and we expect that the proposed experiments to study single ion quantum memories are within reach in the near future. Furthermore, we have developed models for ion-cavity interactions also for multiple ions which can help to readout qubit ion states in an efficient manner.

We are convinced that it remains a promising direction to follow the proposed research also beyond NanOQTech.

References

- [Brachmann13] J. Brachmann, PhD Thesis (2013), LMU Munich [urn:nbn:de:bvb:19-153900](https://nbn-resolving.org/urn:nbn:de:bvb:19-153900)
- [Alnis08] J. Alnis, A. Matveev, N. Kolachevsky, T. Udem, T. W. Hänsch, Phys. Rev. A 77, 053809 (2008).
- [Casabone18] B. Casabone, J. Benedikter, T. Hümmer, F. Oehl, K. de Oliveira Lima, T. W. Hänsch, A. Ferrier, P. Goldner, H. de Riedmatten, D. Hunger, New J. Phys. 20, 095006 (2018)
- [Benedikter19] J. Benedikter, T. Moosmayer, M. Mader, T. Hümmer, D. Hunger, to appear in New Journal of Physics (2019), arxiv:1909.01210
- [Rippe08] L. Rippe, B. Julsgaard, A. Walther, Y. Ying, S. Kröll, Phys. Rev. A 77, 022307 (2008).
- [Roos04] I. Roos, K. Mølmer, Phys. Rev. A 69, 022321 (2004)
- [LeKien00] F. Le Kien, N. H. Quang, K. Hakuta, Opt. Commun. 178 151 (2000)
- [Auffeves07] A. Auffeves, C. Simon, J.-M. Gerard, J.-P. Poizat, Phys. Rev. A 75, 053823 (2007)
- [Lia18] Lia Barbosa Valdetaro, Quantum measurements on Qubits in Optical Cavities, Master Thesis, Aarhus University, 2019. Unpublished, but continuation of project with new student is expected to lead to joint publication of results.
- [Synch19] Kamanasish Debnath, Yuan Zhang, Klaus Mølmer, Collective dynamics of inhomogeneously broadened emitters coupled to an optical cavity with narrow linewidth, submitted for publication: <https://arxiv.org/abs/1904.04877>
- [Suplas18] Kamanasish Debnath, Yuan Zhang, and Klaus Mølmer, Lasing in the superradiant crossover regime Phys. Rev. A 98, 063837 (2018).
- [Suplas19] Yuan Zhang and Klaus Mølmer, Magnetic Field Control of Optical Transmission and Narrow Linewidth Superradiant Lasing by Strontium Atoms; submitted for publication: <https://arxiv.org/abs/1902.06706>